ELSEVIER

Journal of Nuclear Materials 298 (2001) 239–247

journal of nuclear materials

www.elsevier.com/locate/jnucmat

In situ Raman spectroscopic investigation of zirconium–niobium alloy corrosion under hydrothermal conditions

J.E. Maslar *, W.S. Hurst, W.J. Bowers Jr., J.H. Hendricks

Chemical Science and Technology Laboratory, National Institute of Standards and Technology, 100 Bureau Drive, Stop 8360, Gaithersburg, MD 20899-8360, USA

Received 30 April 2001; accepted 11 July 2001

Abstract

In situ Raman spectroscopy was employed to investigate corrosion of a zirconium–niobium alloy in air-saturated water at a pressure of 15.5 MPa and temperatures ranging from 22 to 407 °C in an optically accessible flow cell. Monoclinic ZrO_2 (m-ZrO_2) was identified under all conditions after the coupon was heated to 255 °C for 19 h. Cubic ZrO_2 (c-ZrO_2) was tentatively identified in situ during heating at temperatures between 306 and 407 °C, but was not observed under any other conditions. Species tentatively identified as α-CrOOH and a Cr^{VI} and/or Cr^{III}/Cr^{VI} compound were observed in situ during heating at temperatures between 255 and 407 °C, but were not observed under any other conditions. The chromium compounds were identified as corrosion products released from the optical cell and/or flow system. Published by Elsevier Science B.V.

PACS: 82.80.Ch; 81.70.Fy; 81.65.Mq; 81.05.Bx

1. Introduction

Aqueous metal corrosion at elevated temperatures and pressures is of great importance in systems such as fossil fuel power plants, nuclear power plants, and hydrothermal oxidation reactors. By understanding metal corrosion mechanisms in such systems the adverse effects of corrosion-induced component failure can be minimized. However, component failure is only one important corrosion-related issue. The release of corrosion products and their subsequent transport and deposition is also of significance. Corrosion products can be deposited throughout a reactor system resulting in degradation of system performance, e.g., by creating thermal barriers on heat transfer surfaces or increasing out-of-core radiation fields in nuclear reactors [1,2].

Zirconium-base alloys are of particular interest in aqueous systems at elevated temperatures and pressures. Originally, these alloys were commercially developed primarily for use in nuclear reactors as fuel rod cladding and other core components. However, due to their excellent corrosion resistance, zirconium alloys increasingly are being utilized in additional applications such as chemical processing, e.g., in mineral acids and alkalis in which highly corrosive environments are encountered. Given the technological significance of zirconium alloys, a thorough understanding of their corrosion mechanisms at elevated temperatures and pressures is of broad relevance.

In this investigation, the corrosion of UNS R60705 Zr–Nb alloy in air-saturated water at a pressure of 15.5 MPa and temperatures ranging from 22 to 407 °C was investigated. The nominal composition of UNS R60705 is shown in Table 1. This alloy is the non-nuclear version of the nuclear grade Zr–2.5Nb alloy UNS R60901. The primary difference between the non-nuclear and nuclear grade is the absence of Hf in the nuclear grade alloy, Hf

* Corresponding author. Tel.: +1-301 975 4182; fax: +1-301 869 5924.

E-mail address: jmaslar@nist.gov (J.E. Maslar).

0022-3115/01/$ - see front matter. Published by Elsevier Science B.V.
PII: S0022-3115(01)00657-2

Table 1
Nominal composition of UNS No. R60705 zirconium alloy [3]

Element	Nominal composition, mass percent
Zr+Hf	95.5 min
Hf	4.5 max
Fe+Cr	0.2
Nb	2.5
O	0.18

being removed because it absorbs neutrons whereas zirconium does not. Since Hf has similar aqueous corrosion properties as Zr and since Hf is present at low mass percent in UNS R60705, the presence of Hf in UNS R60705 has little affect on the overall aqueous corrosion resistance of this alloy compared to Hf-free UNS R60901 [4]. Therefore, the corrosion mechanisms observed during exposure of the non-nuclear grade Zr–2.5Nb alloy in this investigation should be nominally identical to corrosion mechanisms which occur during exposure of the nuclear grade Zr–2.5Nb alloy under similar conditions.

For the investigation of corrosion processes at elevated temperatures and pressures, in situ characterization measurements are preferred for a number of reasons. Such measurements potentially can yield a clearer picture of the corrosion mechanisms since the removal of a metal from the corrosion environment can result in modification of the corrosion species. In addition, in situ characterization is necessary to observe transient corrosion products, e.g., resulting from changes in solvent properties due to variations in system temperature and pressure. Also, in the case of nuclear reactors, utilization of in situ measurements can limit the exposure of workers to hazardous radiation. Further, in situ measurement techniques could ultimately be employed for real time process monitoring allowing for more timely maintenance. Due to the experimental constraints of making measurements at elevated temperatures and pressures, many techniques employed to study corrosion are not applicable to in situ investigations. This is not the case for Raman spectroscopy, which also offers the potential for molecular identification, allowing deeper insight into corrosion mechanisms.

A number of ex situ Raman spectroscopic investigations of zirconium alloy aqueous corrosion have been reported [5–21]. However, while a remote Raman spectroscopic system has been described to examine radioactive fuel rod cladding [9], Raman spectroscopy has not been widely applied to in situ investigations of zirconium alloy aqueous corrosion. Therefore, an in situ investigation of zirconium alloy hydrothermal corrosion can provide an enhanced understanding of corrosion mechanisms that are important in many industrial processes.

In this investigation, in situ Raman spectroscopy was employed to observe corrosion products on a Zr–Nb alloy during exposure to air-saturated water at a pressure of 15.5 MPa and temperatures ranging from 22 to 407 °C. In situ Raman spectra were collected at temperatures of ca. 22, 106, 255, 306, and 407 °C as the metal coupon was heated and then cooled. After cooling to room temperature, the coupon was removed from the optical cell and was characterized ex situ with Raman spectroscopy, scanning electron microscopy (SEM), and energy dispersive X-ray spectrometry (EDS).

2. Experimental procedure

For this investigation, an approximately 5 mm × 5 mm × 2 mm thick piece of UNS R60705 Zr–Nb alloy (Teledyne Wah Chang [22]) was cut from a commercially available corrosion test kit coupon. Prior to exposure, the specimen was degreased and polished according to the following: (1) 5 min soak in carbon tetrachloride followed by an acetone rinse and then an isopropanol rinse, (2) polished with 400 grit silicon carbide paper wetted with isopropanol, (3) polished with 600 grit silicon carbide paper wetted with isopropanol, (4) polished with crocus cloth wetted with deionized water, (5) polished with 1 μm aluminum oxide powder and deionized water slurry, (6) 5 min soak in carbon tetrachloride followed by an acetone rinse and then an isopropanol rinse, and (7) a final deionized water rinse. Also used in this study was commercially available ZrO_2 powder (Strem Chemicals) that was employed as obtained to acquire reference Raman spectra. The crystal structure was verified by X-ray diffraction as monoclinic ZrO_2 (m-ZrO_2).

For the corrosion test, the Zr–Nb alloy coupon was placed in an optical cell [23,24] and exposed to deionized, air-saturated water. The water was purified by passage through an ultraviolet oxidizer and ion exchange resin bed. The resulting purified water had a resistivity of 18 MΩ cm or greater and a pH of 5.76, at 21 °C. The water was introduced into the closed flow system at atmospheric pressure and a temperature of 21 °C. Under these conditions, air-saturated water contains about 6.7×10^{-6} standard m^3 of dissolved O_2/kg of H_2O (9.5 ppm). The average system pressure and associated expanded uncertainty with a coverage factor of 2 (based on manufacturer's specifications) was 15.5 ± 0.2 MPa. Exposure temperature was measured with a thermocouple placed on the exterior of the cell. It was estimated that the cell exterior temperature was within 3 °C of the solution temperature during exposures. The length of time the coupon remained at a specific temperature (excluding ramp time) as well as the temperatures at which Raman spectra were collected are summarized in Table 2. The thermocouple reading expanded uncertainty (with a coverage factor of 2) is based on manufacturer's specifications. With a balance of

Table 2
Temperatures at which and exposure times after which in situ Raman spectra were recorded[a]

Temperature (°C)	Total exposure time prior to first measurement at each temperature (h)	Time at each temperature prior to first measurement (h)
22 ± 4.9	17	17
106 ± 5.1	21	4
255 ± 5.5	27	5
255 ± 5.5	41	19
306 ± 5.8	44	2
407 ± 7.3	47.5	3
307 ± 5.8	51.5	3
307 ± 5.8	65	16
256 ± 5.5	69	3
106 ± 5.1	73.5	2
24 ± 4.9	90.5	12

[a] The nominal flow rate was 0.5 ml/min throughout and the coupon was in solution for a total of 91 h.

moderate sensitivity (nominal precision of 0.1–0.2 mg), no difference could be detected in the coupon mass before and after exposure.

The optical cell body was a modified, commercially available 19.05 mm (3/4 in.) union cross tube fitting (Swagelock) made of alloy 600 (UNS No. N06600). One port was occupied by a sample holder assembly, two by window assemblies, and one by an alloy 600 plug, as described previously [23,24]. A Zr–Nb alloy coupon was held in the recess of a sapphire disk by a sapphire washer and alloy 600 mounting hardware so as to electrically insulate the coupon. Each window assembly consisted of a chemical vapor deposited diamond disk (exposed to the solution) adjacent to a sapphire disk, both mounted in an alloy 600 body. Alloy C-276 (UNS No. N10276) tubes were welded to the optical cell for solution introduction and removal.

In situ Raman spectra were generated with 647.1 nm radiation from a krypton ion laser, to minimize (compared to shorter wavelength excitation) interference from potential fluorescent compounds. The ex situ Raman spectra of the corrosion coupon and reference powder presented here were excited with 514.5 nm radiation from an argon ion laser which exhibited higher signal-to-noise ratio than corresponding spectra excited with 647.1 nm radiation (not shown), although otherwise the respective spectra were nominally identical. All spectra were generated in a near-backscattering geometry with appropriate holographic filters (300 cm^{-1} nominal spectral edgewidth and 6.0 nominal optical density), a 0.46 m imaging spectrograph, and a back-illuminated, liquid nitrogen cooled, charge coupled device camera, as previously described [25]. The ZrO_2 powder was manually pressed into a groove in a square aluminum block to facilitate sample handling and spectrum acquisition. For in situ measurements, laser radiation polarized perpendicular to the plane of incidence was focused on the sample with a 150 mm focal length cylindrical lens that produced a rectangular spot approximately 0.2 mm × 2 mm and a power density of less than 19 W/cm^2 at the sample. For ex situ measurements, light was focused on the sample with a 300 mm focal length cylindrical lens that produced an approximately 0.4 mm × 2 mm spot with a corresponding power density of less than 7 W/cm^2 at the sample. For both excitation wavelengths, the instrumental bandpass (FWHM) was ca. 5 cm^{-1} and the instrumental reproducibility was ±2 cm^{-1}. All spectra were obtained in integration times of 10 min or less.

Images of the coupon surface were obtained with a SEM (Hitachi S-4000) operating at a primary electron beam energy of 20 keV. The electron microprobe compositional analysis was performed in the same instrument using EDS (Oxford Instruments) with a primary electron energy of 20 keV. SEM and EDS were performed at several locations on the coupon surface and representative results presented in this paper.

3. Results and discussion

3.1. Ex situ characterization

The SEM images of the exposed corrosion coupon are shown in Fig. 1. These images show relatively thin platelets on the surface of a more extensive underlying film. Such platelets were absent in SEM images of Zr–Nb alloy coupons prior to exposure. Although the chemical composition of the platelets observed in Fig. 1 could not be positively determined, similar platelets observed in the SEM images of 304L stainless steel surfaces exposed under nominally identical conditions in this optical cell and employing this flow system have been tentatively identified as α-CrOOH [26].

The X-ray emission spectrum recorded at a location corresponding to the SEM images is shown in Fig. 2. Peaks due to oxygen, nickel, aluminum, silicon, zirconium, and chromium are observed. X-ray emission

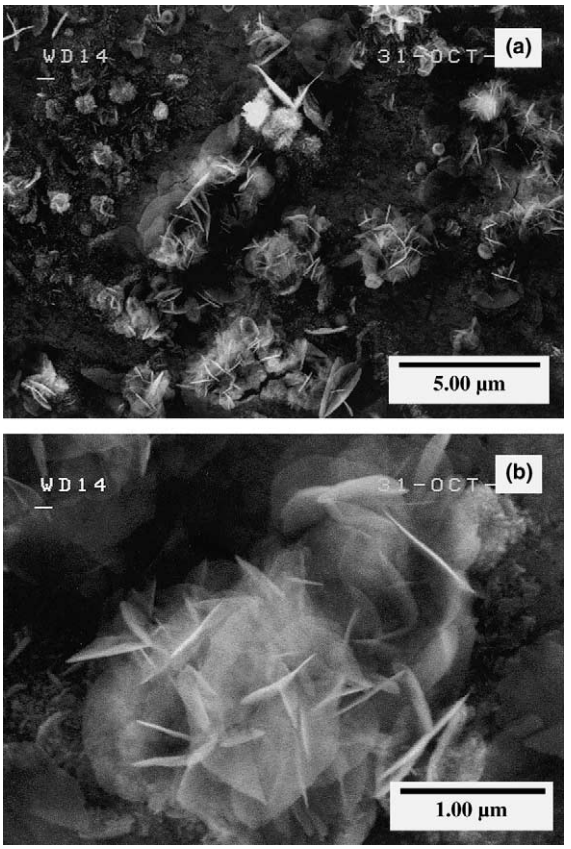

Fig. 1. SEM images of the exposed corrosion coupon at magnifications of (a) 6000× and (b) 30 000×.

spectra of an unexposed, unpolished coupon exhibited only oxygen and zirconium peaks The other elements composing the Zr–Nb alloy either are present at concentrations below the EDS detection limit or their respective signals are unresolved in the presence of the intense zirconium signal. The latter is probably the case for niobium, the major peak of which occurs at 2.16 keV, i.e., on the high energy shoulder of the zirconium peak. The aluminum originates from the sapphire coupon holder. The silicon is due to residual SiC abrasive from the polishing procedure. The nickel and chromium originate from the optical cell and/or flow system which are constructed of alloys 600 and C-276, respectively. The nominal compositions of these alloys are shown in Table 3. Such dissolution of containment materials in water, transport of the resulting corrosion species, and their subsequent deposition at other locations in the system is a widely investigated problem in power reactor coolant loops [1,2].

Fig. 3 shows the ex situ Raman spectra, excited with 514.5 nm radiation, of the exposed coupon and the m-ZrO_2 reference powder. The respective spectral intensities were scaled for comparison. The peak wavenumbers

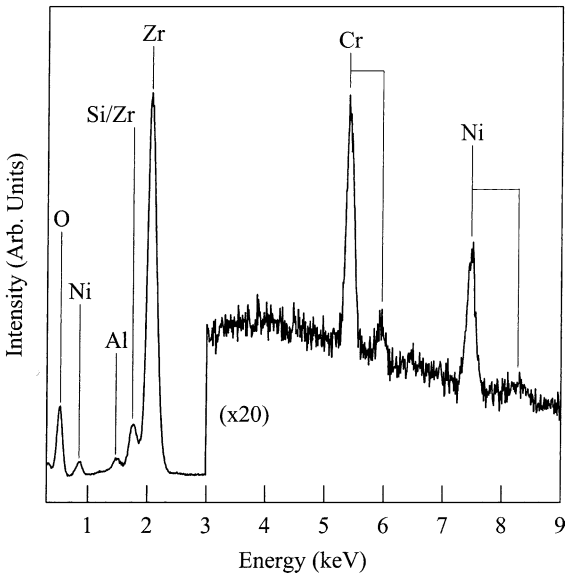

Fig. 2. Exposed corrosion coupon X-ray emission spectrum.

Table 3
Nominal compositions of alloys 600 and C-276 [27]

Element	Nominal composition, mass percent	
	Alloy 600	Alloy C-276
Ni	72.0 min[a]	Balance
Cr	14.0–17.0	14.5–16.5
Fe	6.0–10.0	4.0–7.0
Co	–	2.5 max
Mo	–	15.0–17.0
W	–	3.0–4.5
C	0.15 max	0.02 max
Mn	1.0 max	1.0 max
Si	0.5 max	0.08 max
Cu	0.5 max	–
V	–	0.35 max

[a] Nickel plus cobalt content.

in the reference powder spectrum are summarized in Table 4, in addition to reported nominal Raman shifts of m-ZrO_2, tetragonal ZrO_2 (t-ZrO_2), and cubic ZrO_2 (c-ZrO_2). Features below 160 cm^{-1} are not shown because the coupon spectrum exhibits a background sloping to lower Raman wavenumber and nitrogen and oxygen rotational Raman lines (the spectrum was recorded in air) which preclude the resolution of potential ZrO_2 Raman peaks. m-ZrO_2 is the primary zirconium corrosion species expected to form on zirconium alloys exposed to water at elevated temperatures and pressures [31]. However, the other two ZrO_2 polymorphs also have been identified as corrosion products on zirconium alloys depending on exposure conditions [8]. Since only m-ZrO_2 is stable at atmospheric pressure below ca.

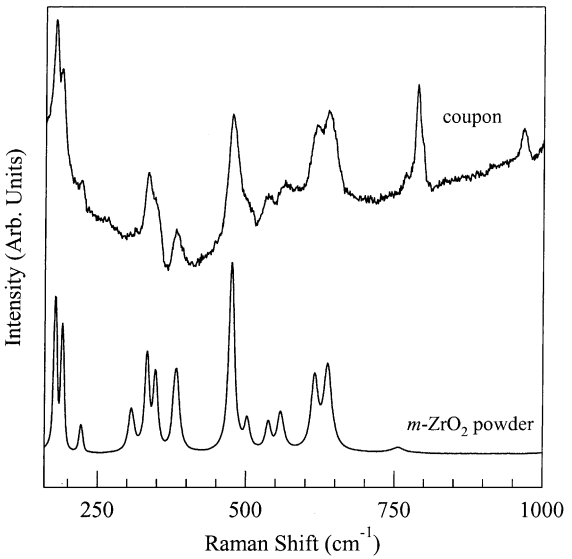

Fig. 3. Ex situ Raman spectra, excited with 514.5 nm radiation, of the exposed coupon and m-ZrO_2 reference powder. The respective spectral intensities are scaled for comparison and the spectra are offset on the vertical scale for clarity.

1205 °C [32], the presence of the other polymorphs is attributed to phase stabilization by film stress, small crystallite size, and/or impurities [8,10,15].

In Fig. 3, the m-ZrO_2 powder peak wavenumbers correspond reasonably well to those observed in the spectrum of the corrosion coupon. However, the peaks in the corrosion coupon spectrum exhibit broader lineshapes and, in some cases, are shifted in wavenumber with respect to the corresponding peaks in the powder spectrum. This is attributed to the Zr–Nb alloy corrosion film having a lower degree of crystallinity than the m-ZrO_2 powder. Differences in crystallite size can result in changes in phonon peak wavenumber, width, and asymmetry with the magnitudes depending on the phonon dispersion [33]. Stress-induced effects, from, e.g., defect- or impurity-induced lattice modification, can have similar effects on the Raman spectra [33]. The peaks at 767 (shoulder), 788, and 967 cm^{-1} in the corrosion coupon spectrum are attributed to SiC [34]. Although chromium and nickel are detected by EDS, there is no evidence of chromium or nickel species in the ex situ Raman spectrum. This could be due to a number of factors. The corrosion product could exhibit weak Raman-active modes, e.g., possess low crystallinity, or none at all, or the corrosion product could be present in low concentrations. Although the chemical form of the respective corrosion product could not be determined, e.g., whether chromium and nickel are incorporated into ZrO_2 as impurities or exist as discrete nickel and/or chromium oxides, SEM results suggest that at least some chromium is present as α-CrOOH, as discussed previously.

While only m-ZrO_2 is positively identified in the coupon spectrum in Fig. 3, the broad lineshapes and background make it difficult to rule out the presence of

Table 4
Nominal Raman wavenumbers (cm^{-1}) of ZrO_2 polymorphs

Monoclinic (this work)[a]	Monoclinic [28][b]	Tetragonal [29][b]	Cubic [29][b]	Stabilized cubic [30][b]
756	757			
637	638	640		
616	616	615		
				600[c]
558	558	561		
538	539	536		
502	503			
			490[c]	
475	476	473		
	385			
382	380	380		
347	349			
333	334	332		
307	308			
		263		
222	224	223		
190	192	189		
178	180	179		
		148		
102	105			

[a] The wavenumber of a well-resolved peak has an associated uncertainty of ±2 cm^{-1}.
[b] No assertions are made in this work concerning the uncertainties associated with the Raman wavenumbers reported in the literature.
[c] Broad.

the other zirconia polymorphs. t-ZrO_2 can be identified by the presence of features at ca. 148 and 263 cm^{-1} (see Table 4). However, the 263 cm^{-1} feature is observed at wavenumbers as high as ca. 280 cm^{-1} in t-ZrO_2 formed during corrosion of zirconium alloys [5,35]. Further complicating the potential identification of t-ZrO_2 is the presence of weak spectral artifacts in the ca. 260 and 270 cm^{-1} wavenumber range due to the holographic notch filters employed in this work. c-ZrO_2 can be identified by broad features at ca. 490 and ca. 600 cm^{-1} for pure and stabilized c-ZrO_2, respectively. However, as with t-ZrO_2, the broad lineshapes and background in the corrosion coupon spectrum potentially interfere with the resolution of c-ZrO_2 features.

3.2. In situ characterization

Fig. 4 shows the in situ Raman spectra of the Zr–Nb alloy coupon as it was (a) heated to 407 °C and (b) cooled to 24 °C. Spectra recorded below 255 °C while heating were nominally identical to the spectrum obtained after 5 h at 255 °C and, therefore, omitted for clarity. The 407 °C spectrum is the same in Fig. 4(a) and (b). In Fig. 4(b), the spectrum of the coupon at 307 °C was taken after 3 h at temperature. The spectrum collected at 307 °C after 16 h at temperature was nominally identical to the spectrum collected after 3 h at 307 °C and, therefore, the spectrum collected after 16 h was omitted for clarity. The peak wavenumbers of m-ZrO_2 (m), t-ZrO_2 (t), and c-ZrO_2 (c) are indicated. The weak feature observed at 418 cm^{-1} in these spectra originates from the sapphire window [36]. Peaks observed at 789 and 969 cm^{-1} are due to SiC. No evidence of passivation/corrosion layer species is observed in the spectra collected after 5 h at 255 °C and at lower temperatures during the heating cycle. This is attributed to the passivation/corrosion layer being insufficiently thick and/or crystalline to be detected.

m-ZrO_2 features are first observed in the spectrum obtained after 19 h at 255 °C and become more apparent in subsequent spectra. In all spectra, m-ZrO_2 features generally exhibit low intensities and broad lineshapes, as observed in the ex situ Raman spectrum. These results indicate that, although the corrosion film thickness and/or crystallinity is increasing with increasing exposure times and temperatures, the corrosion film is always relatively thin and/or disordered. While it is difficult to determine the presence or absence of the other ZrO_2 polymorphs due to the low peak intensities, broad peak lineshapes, and water Raman scattering background in the corrosion coupon spectra, the broad feature at ca. 600 cm^{-1} is tentatively assigned to stabilized c-ZrO_2. Such a feature is absent in coupon spectra during cooling. Assuming that c-ZrO_2 is the origin of this feature, its absence in subsequent spectra indicates that the mechanism responsible for c-ZrO_2 stabilization is no longer operative. It has been reported that in corrosion films stress-stabilized t-ZrO_2 transforms to m-ZrO_2 when the film reaches a thickness sufficient to relax the

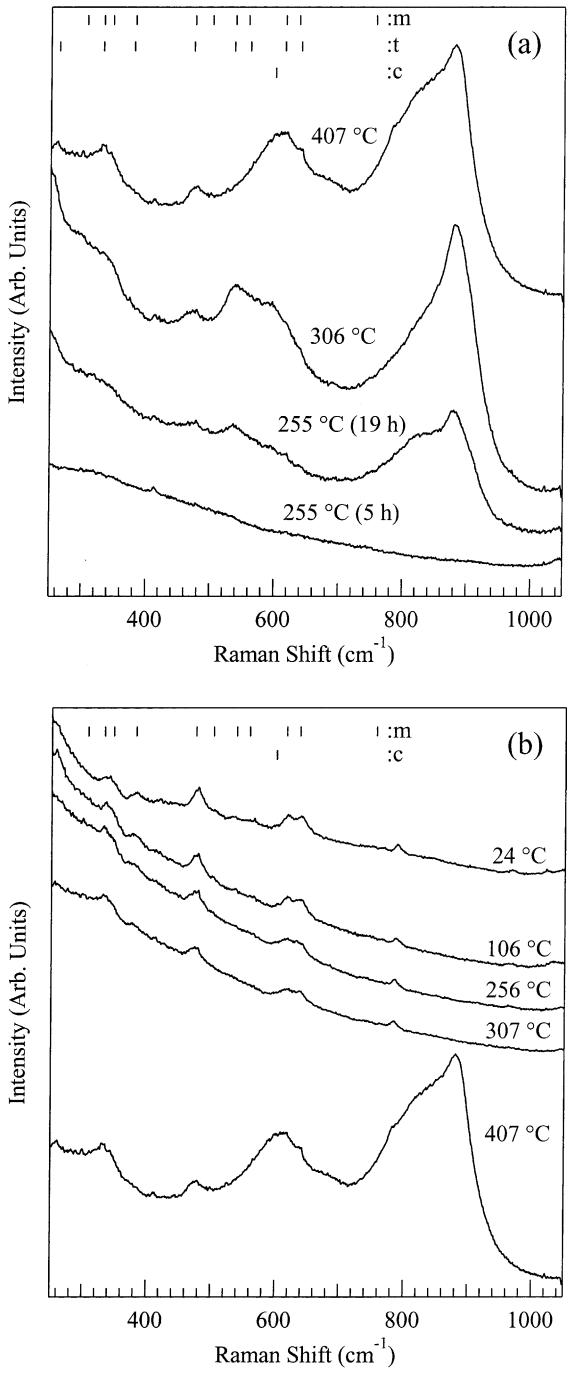

Fig. 4. In situ Raman spectra recorded as the coupon was (a) heated to 407 °C and (b) cooled to 24 °C. The spectra are offset on the vertical scale for clarity and the time is the total time elapsed at a particular temperature. The Raman wavenumbers of m-ZrO_2 (m), t-ZrO_2 (t), and c-ZrO_2 (c) are indicated.

film stress [12]. Perhaps a similar mechanism is occurring here in which relaxation of film stress results in transformation of the observed c-ZrO_2 to m-ZrO_2 or another zirconia polymorph which cannot be identified in the Raman spectra. As mentioned above, it is difficult to determine the presence or absence t-ZrO_2, which can be identified by the presence of a peak in the ca. 263–280 cm^{-1} range. A number of in situ Raman spectra exhibit weak features in this wavenumber range. However, based on comparison to other unpublished spectra recorded in the course of this investigation, these features are attributed to an artifact from the holographic notch filter rather than t-ZrO_2.

The spectra of the coupon at 255, 306, and 407 °C during heating exhibit a number of features indicating the presence of species other than ZrO_2 polymorphs. Fig. 5 shows these Raman spectra with the m-ZrO_2 features removed. m-ZrO_2 features were removed by subtracting the spectrum collected at a particular temperature while the coupon was cooled (these spectra exhibit only m-ZrO_2 features) from the corresponding spectrum collected at nearly the same temperature as the coupon was heated. The 307 °C spectrum that was collected as the coupon was cooled was subtracted from both the 306 °C and 407 °C spectra that were collected during heating. Subtraction was done after normalizing the 478 cm^{-1} m-ZrO_2 peak in each spectrum obtained during cooling to the corresponding peak in the spectrum obtained at the corresponding temperature during heating. Unambiguous peak assignment is difficult due to the poor resolution in these spectra, however, tentative assignments can be made.

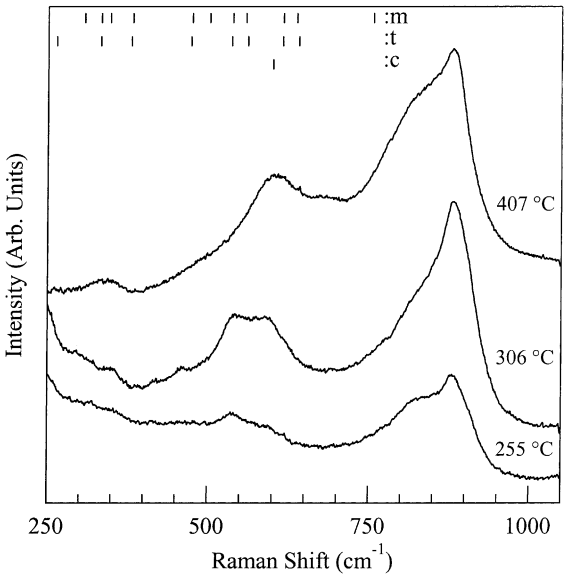

Fig. 5. In situ Raman spectra of the coupon during heating at 255, 306, and 407 °C with the m-ZrO_2 features subtracted. The Raman wavenumbers of m-ZrO_2 (m), t-ZrO_2 (t), and c-ZrO_2 (c) are indicated.

The Raman spectral features of the non-zirconia species observed in Fig. 5 are very similar to Raman features observed during investigations of chromium and nickel corrosion [25,37]. In those studies, coupons were exposed in this optical cell and employed this flow system under exposure conditions quite similar to those of this Zr–Nb alloy. The Raman features in the chromium and nickel investigations were attributed to various chromium species that originated as corrosion products released from the optical cell and/or flow system. Chromium species are most likely because alloys such as those of which the optical cell and flow system are fabricated preferentially release chromium in oxygenated water at intermediate pH and at temperatures up to at least ca. 300 °C [38–41]. The mechanism is the oxidation of the Cr^{III}-containing protective scales on the structural alloys, e.g., Cr_2O_3 and CrOOH, to soluble Cr^{VI}-containing species such as CrO_4^{2-}, $Cr_2O_7^{2-}$, $HCrO_4^-$, and H_2CrO_4 (depending on such factors as pH and solvent density) [41–44]. These Cr^{VI} species are then transported in solution and deposited on surfaces via reaction and/or adsorption mechanisms involving surface hydroxyl groups [45].

The most intense peaks in Fig. 5 are observed in the 800–900 cm^{-1} range with the maximum intensity at ca. 880 cm^{-1} and a shoulder at ca. 825 cm^{-1}. Assuming a chromium species is responsible, chromium oxide features in this wavenumber range generally are attributed to Cr^{VI}-oxygen terminal stretching modes or mixed Cr^{III}/Cr^{VI} oxide vibrational modes [46]. Hydrated surface chromate species have been reported to exhibit a vibrational mode at ca. 865 cm^{-1} [47]. The most intense peak in the aqueous $HCrO_4^-$ Raman spectrum is reported from ca. 880 to 899 cm^{-1} [48–50]. A number of mixed Cr^{III}/Cr^{VI} oxides have been identified during the thermal decomposition of various chromium-containing materials [51–53]. Crystalline Cr^{III}/Cr^{VI} compounds such as Cr_3O_8, Cr_2O_5, and XCr_3O_8 (X = Na, K, Rb) exhibit their most intense Raman spectral features in the ca. 820–904 cm^{-1} range at room temperature [46,54]. The most intense Raman spectral feature of an amorphous Cr^{III}/Cr^{VI} compound has been observed at 859 cm^{-1} [55]. The presence of a Cr^{VI} or crystalline Cr^{III}/Cr^{VI} species would also account for the weak features observed in the 340–350 cm^{-1} range in the spectra of the coupon at 306 and 407 °C. Unfortunately, the broad Raman spectral lineshapes and lack of reference spectra precludes assignment of the peaks, as well as even the distinction between a Cr^{VI} or Cr^{III}/Cr^{VI} species.

The three Raman spectra in Fig. 5 also exhibit features in the ca. 520–620 cm^{-1} range. A single broad peak is observed centered at ca. 603 cm^{-1} in the spectrum collected at 407 °C, while multiple, unresolved peaks are observed in the 540–630 cm^{-1} range in the spectra

obtained at the lower two temperatures. As discussed above, the ca. 603 cm^{-1} is attributed to c-ZrO_2. The features in the spectrum of the coupon at 255 °C after 19 h are attributed to α-CrOOH [25]. Features in the 540–630 cm^{-1} range in the spectrum collected at 306 °C are also attributed to α-CrOOH. These features are more intense than those observed in the spectrum collected at 255 °C after 19 h. This is attributed to the presence of unresolved scattering from c-ZrO_2 at ca. 603 cm^{-1}.

The features attributed to chromium corrosion products are observed only in situ when heating and are absent when the coupon is cooled. These results suggest that corrosion product deposition is not entirely due to a temperature-induced change in water properties (e.g., ion product, density, or dielectric constant) or deposition also should be observed as the coupon is cooled. One factor that is different in the heating and cooling cycles is the surface of the Zr–Nb alloy coupon. The amount of ZrO_2 on the surface increases with exposure time. These results suggest that the hydrated Zr–Nb alloy surface interacts differently with soluble chromium corrosion species than does the hydrated ZrO_2 surface. However, the mechanism is uncertain. Possibly, the presence of ZrO_2 inhibits the deposition of chromium species or facilitates a redox reaction that produces a chromium specie(s) with lower Raman scattering efficiency.

4. Conclusions

A Zr–Nb alloy coupon was exposed to air-saturated water at a pressure of 15.5 MPa and temperatures ranging from 22 °C to 407 °C. m-ZrO_2 was identified under all conditions after the coupon was heated to 255 °C for 19 h. c-ZrO_2 also was tentatively identified in situ at temperatures between 306 and 407 °C, but was not observed under subsequent conditions. In addition, deposition of corrosion species released from the optical cell and/or flow system was observed in situ and at temperatures between 255 and 407 °C. The species were tentatively identified as α-CrOOH and a Cr^{VI} and/or Cr^{III}/Cr^{VI} species. The features due to these species were absent from the in situ Raman spectra obtained as the coupon was cooled as well as the ex situ Raman spectra. These results indicate that the Zr–Nb alloy surface interacts with released chromium corrosion species differently before and after ZrO_2 film formation.

Acknowledgements

The authors gratefully acknowledge R. Sutherlin and C.M. Eucken of Wah Chang, Albany, OR for helpful discussions, M.I. Aquino for performing X-ray diffraction measurements on the zirconia powder, and W.E. Allmon of Framatome Technologies, Inc., Lynchburg, VA and from McDermott Technology, Inc. (Babcock & Wilcox), Alliance, OH for calculations of the O_2 content of air-saturated water. This research was conducted while J.H.H. held a NIST National Research Council postdoctoral Fellowship.

References

[1] D.H. Lister, Nucl. Energy – J. Br. Nucl. Energy Soc. 32 (1993) 103.
[2] D.H. Lister, R.D. Davidson, E. McAlpine, Corros. Sci. 27 (1987) 113.
[3] J.R. Davis (Desk Ed.), Metals Handbook, 2nd Ed., ASM International, Materials Park, OH, 1998, p. 621.
[4] C.M. Eucken, Wah Chang, Albany, OR, Personal communication.
[5] P. Barbéris, T. Merle-Méjean, P. Quintard, J. Nucl. Mater. 246 (1997) 232.
[6] B. Cox, C.G. Wu, J. Nucl. Mater. 199 (1993) 272.
[7] T.E. Doyle, J.L. Alvarez, in: A.D. Romig Jr., J.I. Goldstein (Eds.), Microbeam Analysis, 1984: Proceedings of the 19th Annual Conference of the Microbeam Analysis Society, Bethlehem, PA, USA, July 16–20, 1984, San Francisco, CA, 1984, p. 103.
[8] T.E. Doyle, J.L. Alvarez, in: R.L. Snyder, R.A. Condrate Sr., F. Johnson (Eds.), Advances in Materials Characterization, II (Materials science research; vol. 19), Plenum, New York, 1985, p. 155.
[9] H.G.M. Edwards, D.A. Long, I.T. Willis, J. Raman Spectrosc. 26 (1995) 757.
[10] J. Godlewski, in: A.M. Garde, E.R. Bradley (Eds.), Zirconium in the Nuclear Industry: Tenth International Symposium, ASTM STP 1245, Baltimore, MD, USA, June 21–24, 1993, American Society for Testing and Materials, Philadelphia, PA, 1994, p. 663.
[11] J. Godlewski, P. Bouvier, G. Lucazeau, L. Fayette, in: G.P. Sabol, G.D. Moan (Eds.), Zirconium in the Nuclear Industry: Twelfth International Symposium, ASTM STP 1354, Toronto, Canada, January 15–18, 1998, American Society for Testing and Materials, West Conshohocken, PA, 2000, p. 877.
[12] J. Godlewski, J.P. Gros, M. Lambertin, J.F. Wadier, H. Weidinger, in: C.M. Eucken, A.M. Garde (Eds.), Zirconium in the Nuclear Industry: Ninth International Symposium, ASTM STP 1132, Kobe, Japan, November 5–8, 1990, American Society for Testing and Materials, Philadelphia, PA, 1991, p. 416.
[13] H.S. Hong, S.J. Kim, K.S. Lee, J. Nucl. Mater. 238 (1996) 211.
[14] H.S. Hong, S.J. Kim, K.S. Lee, J. Nucl. Mater. 273 (1999) 177.
[15] J. Krýsa, J. Maixner, P. Matějka, V. Vrtílková, Mater. Chem. Phys. 63 (2000) 1.
[16] Y.P. Lin, O.T. Woo, D.J. Lockwood, in: K. Barmak, M.A. Parker, J.A. Floro, R. Sinclair, D.A. Smith (Eds.), Polycrystalline Thin Films: Structure, Texture, Properties, and Applications, 343, San Francisco, CA, 1994, Materials Research Society, Pittsburgh, PA, p. 487.

[17] J. Maixner, J. Krýsa, P. Matějka, V. Vrtílková, Mater. Sci. Forum 321–324 (2000) 737.
[18] J.S. Moya, M. Diaz, J.F. Bartolomé, E. Roman, J.L. Sacedon, J. Izquierdo, Acta Mater. 48 (2000) 4749.
[19] C. Miyake, A. Nakatani, T. Isobe, J. Nucl. Mater. 217 (1994) 172.
[20] D. Pecheur, J. Godlewski, J. Peybernes, L. Fayette, M. Noe, A. Frichet, O. Kerrec, in: G.P. Sabol, G.D. Moan (Eds.), Zirconium in the Nuclear Industry: Twelfth International Symposium, ASTM STP 1354, Toronto, Canada, 2000, ASTM, West Conshohocken, PA, p. 793.
[21] O.T. Woo, D.J. Lockwood, Y.P. Lin, V.F. Urbanic, in: D.A. Bonnell, M. Rühle, U. Chowdhry (Eds.), Structure and Properties of Interfaces in Ceramics, vol. 357, Boston, MA, 1995, Materials Research Society, Pittsburgh, PA, p. 219.
[22] Certain commercial equipment, instruments, and materials are identified in this publication to adequately specify the experimental procedure. Such identification in no way implies approval, recommendation, or endorsement by the National Institute of Standards and Technology, nor does it imply that the equipment, instruments, or materials identified are necessarily the best available for the purpose.
[23] W.S. Hurst, M.S. Hodes, W.J. Bowers Jr., V.E. Bean, J.E. Maslar, K.A. Smith, J. Supercrit. Fluids (2001), in press.
[24] J.E. Maslar, W.S. Hurst, W.J. Bowers, J.H. Hendricks, M.I. Aquino, J. Electrochem. Soc. 147 (2000) 2532.
[25] J.E. Maslar, W.S. Hurst, W.J. Bowers Jr., J.H. Hendricks, M.I. Aquino, I. Levin, Appl. Surf. Sci. 180 (2001) 102.
[26] J.E. Maslar, W.S. Hurst, W.J. Bowers Jr., J.H. Hendricks, Corrosion (2001), to be submitted for publication.
[27] J.R. Davis (Desk Ed.), Metals Handbook, 2nd Ed., ASM International, Materials Park, OH, 1998, p. 609.
[28] B.-K. Kim, H.-O. Hamaguchi, Phys. Status Solidi B 203 (1997) 557.
[29] C.M. Phillippi, K.S. Mazdiyasni, J. Am. Ceram. Soc. 54 (1971) 254.
[30] J.G. Cai, C. Raptis, Y.S. Raptis, E. Anastassakis, Phys. Rev. B – Condens. Matter 51 (1995) 201.
[31] F. Garzarolli, H. Seidel, R. Tricot, J.P. Gros, in: C.M. Eucken, A.M. Garde (Eds.), Zirconium in the Nuclear Industry: Nineth International Symposium, ASTM STP 1132, Kobe, Japan, November 5–8, 1990, American Society for Testing and Materials, Philadelphia, PA, 1991, p. 395.
[32] J.P. Abriata, J. Garcés, R. Versaci, Bull. Alloy Phase Diag. 7 (1986) 116.
[33] P.M. Fauchet, in: D.J. Lockwood, J.F. Young (Eds.), Light Scattering in Semiconductor Structures and Superlattices, Plenum, New York, 1991, p. 229.
[34] S. Nakashima, H. Harima, Phys. Status Solidi A 162 (1997) 39.
[35] P. Barbéris, G. Corolleur-Thomas, R. Guinebretière, T. Merle-Mejéan, A. Mirgorodsky, P. Quintard, J. Nucl. Mater. 288 (2001) 241.
[36] S.P.S. Porto, R.S. Krishnan, J. Chem. Phys. 47 (1967) 1009.
[37] J.E. Maslar, W.S. Hurst, W.J. Bowers Jr., J.H. Hendricks, M.I. Aquino, Corrosion (2001), submitted for publication.
[38] Y. Hemmi, Y. Uruma, N. Ichikawa, J. Nucl. Sci. Technol. 31 (1994) 443.
[39] T. Honda, A. Minato, M. Izumiya, K. Ohsumi, H. Matsubayashi, J. Nucl. Sci. Technol. 20 (1983) 871.
[40] T. Honda, M. Izumiya, A. Minato, K. Ohsumi, H. Matsubayashi, Nucl. Technol. 64 (1984) 35.
[41] E. McAlpine, D.H. Lister, H. Ocken, Mater. Perform. 24 (1985) 33.
[42] P. Kritzer, N. Boukis, E. Dinjus, J. Mater. Sci. Lett. 18 (1999) 1845.
[43] P. Kritzer, N. Boukis, E. Dinjus, J. Supercrit. Fluids 15 (1999) 205.
[44] N. Spanos, S. Slavov, C. Kordulis, A. Lycourghiotis, Langmuir 10 (1994) 3134.
[45] H. Hohl, L. Sigg, W. Stumm, in: M.C. Kavanaugh, J.O. Leckie (Eds.), Particulates in Water: Characterization, Fate, Effects, and Removal, Advances in Chemistry Series 189, American Chemical Society, Washington, DC, 1980, p. 1.
[46] J.E. Maslar, W.S. Hurst, T.A. Vanderah, I. Levin, J. Raman Spectrosc. 32 (2001) 201.
[47] B.M. Weckhuysen, I.E. Wachs, R.A. Schoonheydt, Chem. Rev. 96 (1996) 3327.
[48] J.B.B. Heyns, J.J. Cruywagen, K.T. Carron, J. Raman Spectrosc. 30 (1999) 335.
[49] G. Michel, R. Machiroux, J. Raman Spectrosc. 14 (1983) 22.
[50] J.D. Ramsey, R.L. McCreery, J. Electrochem. Soc. 146 (1999) 4076.
[51] B. Kubota, J. Am. Ceram. Soc. 44 (1961) 239.
[52] C.N.R. Rao, G.V. Subba Rao, Transition Metal Oxides Crystal, Chemistry Phase Transition and Related Aspects, vol. NBS-NSRDS 49, United States Government, Washington, DC, 1974, p. 50.
[53] K.A. Wilhelmi, Acta Chem. Scand. 22 (1968) 2565.
[54] M.J. Saavedra, C. Parada, E.J. Baran, J. Phys. Chem. Solids 57 (1996) 1929.
[55] L. Xia, R.L. McCreery, J. Electrochem. Soc. 145 (1998) 3083.